

Collaborative framework for PIV uncertainty quantification: the experimental database

This content has been downloaded from IOPscience. Please scroll down to see the full text.

2015 Meas. Sci. Technol. 26 074003

(<http://iopscience.iop.org/0957-0233/26/7/074003>)

View [the table of contents for this issue](#), or go to the [journal homepage](#) for more

Download details:

This content was downloaded by: asciacchitano

IP Address: 131.180.16.53

This content was downloaded on 30/05/2016 at 14:20

Please note that [terms and conditions apply](#).

Collaborative framework for PIV uncertainty quantification: the experimental database

Douglas R Neal¹, Andrea Sciacchitano², Barton L Smith³ and Fulvio Scarano²

¹ LaVision Inc., Ypsilanti, MI 48197, USA

² Aerospace Engineering Department, Delft University of Technology, Delft, The Netherlands

³ Department of Mechanical and Aerospace Engineering, Utah State University, Logan, UT 84322, USA

E-mail: dneal@gmx.com

Received 21 November 2014, revised 27 January 2015

Accepted for publication 10 February 2015

Published 5 June 2015



CrossMark

Abstract

The uncertainty quantification of particle image velocimetry (PIV) measurements has recently become a topic of great interest as shown by the recent appearance of several different methods within the past few years. These approaches have different working principles, merits and limitations, which have been speculated upon in subsequent studies. This paper reports a unique experiment that has been performed specifically to test the efficacy of PIV uncertainty methods. The case of a rectangular jet, as previously studied by Timmins *et al* (2012) and Wilson and Smith (2013b), is used. The novel aspect of the experiment is simultaneous velocity measurements using two different time-resolved PIV systems and a hot-wire anemometry (HWA) system. The first PIV system, called the PIV measurement system ('PIV-MS'), is intended for nominal measurements of which the uncertainty is to be evaluated. It is based on a single camera and features a dynamic velocity range (*DVR*) representative of typical PIV experiments. The second PIV system, called the 'PIV-HDR' (high dynamic range) system, features a significantly higher *DVR* obtained with a higher digital imaging resolution. The hot-wire is placed in close proximity to the PIV measurement domain. The three measurement systems were carefully set to simultaneously measure the flow velocity at the same time and location. The comparison between the PIV-HDR system and the HWA provides an estimate of the measurement precision of the reference velocity for evaluation of the instantaneous error in the measurement system. The discrepancy between the PIV-MS and the reference data provides the measurement error, which is later used to assess the different uncertainty quantification methods proposed in the literature. A detailed comparison of the uncertainty estimation methods based on the present datasets is presented in a second paper from Sciacchitano *et al* (2015). Furthermore, this database offers the potential to be used for comparison of the measurement accuracy of existing or newly developed PIV interrogation algorithms. The database is publicly available on the website www.piv.de/uncertainty.

Keywords: particle image velocimetry, uncertainty quantification, hot-wire anemometry, fluid dynamics

(Some figures may appear in colour only in the online journal)

1. Introduction

The widespread use of particle image velocimetry (PIV) for fluid velocity measurements has motivated better understanding and estimation of the errors associated with the technique. Applications of PIV are diverse and include areas

where uncertainty estimates are required, such as validation of computational fluid dynamics (CFD) models and obtaining regulatory approval for new product designs (e.g. in the biomedical sector). Realistic uncertainty estimates would also improve the credibility of PIV in areas where it is less commonly accepted, as in industrial facilities.

Measurement errors are typically defined as the difference between the measured value and the true value (Coleman and Steele 2009) and can be categorized as bias errors, which remain fixed for constant inputs, and random errors, which vary in time. It is worth clarifying that although the terms error and uncertainty are closely related, they are not synonymous. The uncertainty quantification (UQ) of an experimental measurement is the practice of estimating the range over which one expects to find the error. These estimates are usually probability-based and often expressed as a confidence interval. Since PIV is a whole-field instantaneous technique, the propagation of the uncertainty from the instantaneous velocity components (2 or 3 depending on the experimental setup) to the commonly used derivatives (e.g. vorticity) and their associated statistics (mean, standard deviation, covariance, etc.) is of great interest in the fluid dynamics community. A PIV measurement involves many steps, where numerous error sources can play a role and often interact. Among those, the most relevant are noise in the recordings (Huang *et al* 1997), out-of-plane motion (Nobach and Bodenschatz 2009), peak-locking due to small particle images (Westerweel 1997, Christensen 2004) and velocity gradients (Meunier and Leweke 2003, Westerweel 2008). Also particle image diameter, sub-pixel displacement and image density play a role on the measurement precision (Westerweel 2000). All these errors can be mitigated or exacerbated depending on the choice of seeding tracers, illumination sources, digital recording, image pre-processing and interrogation algorithms. This concurrence of parameters makes quantifying PIV uncertainty a non-trivial task.

Initial works on PIV accuracy used Monte Carlo simulations (Keane and Adrian 1992, Lecordier *et al* 2001, Raffel *et al* 2007) where synthetic images were analyzed. The use of computer simulated experiments has the clear advantage that the exact value of each velocity vector is known and quantifying the measurement error becomes straightforward. However, the limitations of using synthetic images have been well understood and highlighted in a number of collaborative works (see, for instance, the 2nd PIV and 3rd PIV challenges, Stanislas *et al* 2005 and Stanislas *et al* 2008).

As a result, there is a clear need to estimate PIV uncertainty from actual experiments, which has resulted in several studies within the past few years that devised new methods to approach uncertainty quantification. Each method has the same objective of estimating PIV uncertainty from a given experiment previously realized (*a-posteriori*), but the proposed approaches vary to a significant extent. The methods are briefly recalled here and explained in further detail in a related article from Sciacchitano *et al* (2015). The four uncertainty techniques are presented in order of their appearance in the literature:

- (a) The uncertainty surface method (Timmins *et al* 2012) uses a 4D response surface (assuming four error sources) that is specific to the PIV algorithm.
- (b) The particle disparity method (Sciacchitano *et al* 2013) takes the measured velocity as a predictor to match the particle images between an image pair.

- (c) The peak ratio method (Charonko and Vlachos 2013) associates the ratio of primary to secondary peak height in the correlation map with the experimental uncertainty.
- (d) The correlation statistics method (Wieneke 2015) uses a statistical analysis of the intensity patterns in the image pairs.

The above works have motivated the need for a collaborative framework to examine the adequacy of these techniques, as well as of new ones yet to be developed. Since these methods are each based on an *a-posteriori* approach, an experimental set of PIV data is required that can provide appropriate test conditions to evaluate each of the methods. The main effort is to realize an experiment where the velocity is measured along with its true value. The latter not being attainable, the problem translates into a measurement of the velocity with significant higher measurement precision to establish a reliable reference velocity. This is achieved using two different measurement techniques, PIV and hot-wire anemometry (HWA), as described in detail in the following sections.

The use of HWA as a reference measurement technique to assess the performance of PIV is not new. Saarenrinne *et al* (2001) and Lavoie *et al* (2007) conducted experiments in turbulent flows to investigate the effect of the PIV spatial resolution on statistical quantities such as Reynolds stresses and turbulence energy dissipation. In both cases, PIV and HWA systems were not operated simultaneously because only statistical quantities were investigated. Along a similar line, Wilson and Smith (2013b) used a single hot-wire probe to statistically compare with PIV data at the same location. Sciacchitano *et al* (2013), instead, evaluated the reference velocity using an advanced interrogation method for time-resolved PIV data.

The present study improves on the previous efforts by allowing a direct estimate of the instantaneous measurement error of the PIV data. The instantaneous error is required for all the applications where the flow dynamics are investigated, e.g. in transient and unsteady flows. The flow velocity is measured simultaneously using three independent systems: two separate PIV systems and a HWA system. The first PIV system, called the PIV measurement system ('PIV-MS'), delivers data for which the uncertainty is to be evaluated. The system is based on a single camera (2C-PIV) and features a dynamic velocity range (*DVR*) representative of typical PIV experiments. The second PIV system, called the 'PIV-HDR' (high dynamic range) system, is composed of two cameras in stereoscopic configuration and features a significantly higher *DVR* obtained with a higher digital imaging resolution. Finally, the hot-wire is placed close to the edge of the illuminated domain such to be able to compare the results with PIV measurements with minimal corrections. All three of the measurement systems were carefully set to simultaneously collect time-resolved data. Since the HWA and PIV-HDR data are meant to serve as reference for the PIV-MS, their measurement uncertainty is previously assessed here and the suitability for assessing uncertainty estimation methods is discussed. The present database has also been intended to be used for additional applications for assessing advanced PIV algorithms (Stanislas *et al* 2005, 2008), particularly those focused

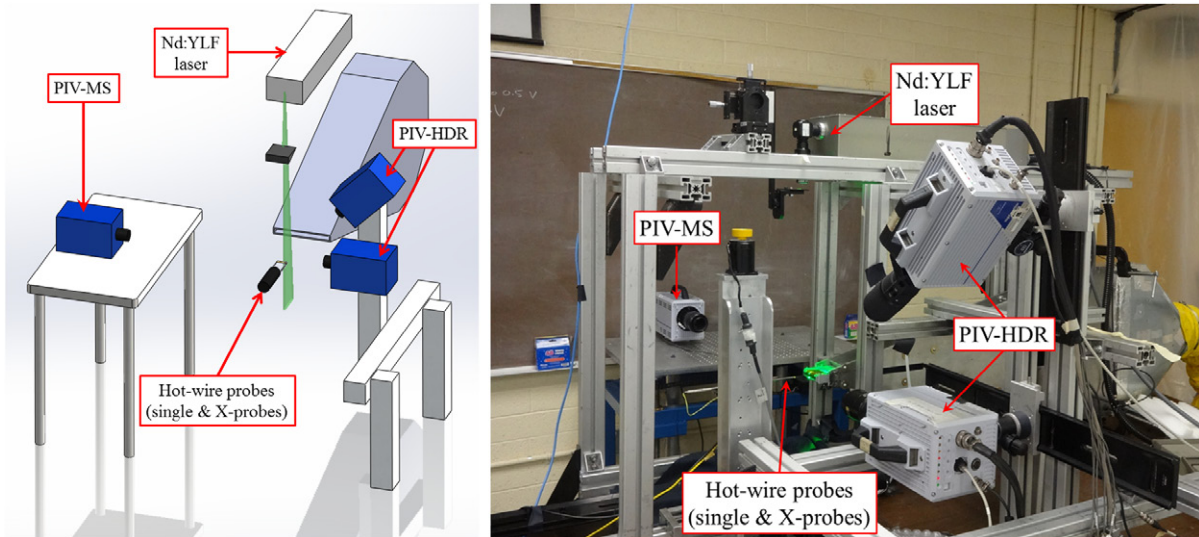


Figure 1. The experimental setup (left: schematic view; right: actual view).

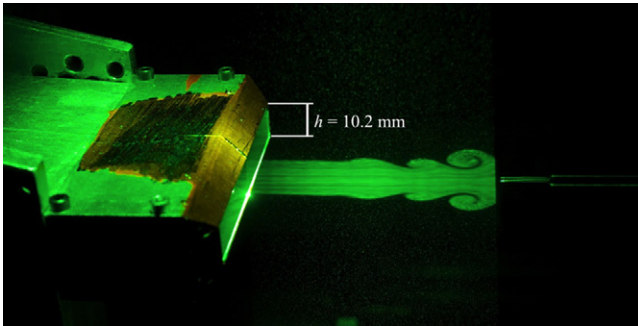


Figure 2. Flow visualization of steady and unsteady jet core region.

on extending the dynamic range of TR-PIV (Hain and Kähler 2007, Sciacchitano *et al* 2012, Lynch and Scarano 2013).

2. Experimental setup

The experiments were conducted in the Experimental Fluid Dynamics Laboratory (EFDL) at Utah State University, where a rectangular jet used by Timmins *et al* (2012) and Wilson and Smith (2013b) is operated. The jet facility has a rectangular nozzle of aspect ratio 7.2, based on a width of 72.8 mm and a height $h = 10.2$ mm. The jet Reynolds number is defined as

$$Re_h = \frac{\rho u_o h}{\mu} \quad (1)$$

where u_o represents the inviscid jet core velocity and ρ and μ are the air density and dynamic viscosity, respectively. Most experiments were conducted with $u_o = 5 \text{ m s}^{-1}$, which yields $Re_h = 3000$ (note that Wilson and Smith based the Reynolds number in the experiments on the jet half-height). The data were acquired at various sampling rates in the range 4–10 kHz and all three of the measurement systems were synchronized to yield simultaneous measurements. A schematic illustration of the experimental setup with the jet and the measurement systems is shown in figure 1(left). Further details are given in the corresponding photo (figure 1(right)).

A light-sheet visualization of the jet in the laminar region is given in figure 2, where also the position of the hot-wire is visible at the edge of the PIV measurement domain. The jet begins in the laminar regime ($x/h = 0$) and shear layer instabilities are visualized from $x/h > 4$. The time-averaged velocity field in the jet median plane gives an overview of the jet spatial development and the adopted measurement coordinate system (figure 3). The number of distinct flow regimes along different regions makes this jet an excellent case for a generalized assessment of PIV uncertainty. These regions are described in detail in section 5.

3. Experimental techniques

The three measurement systems and their specifications are described in detail in the sections below. An example of comparison of measurement regions of the three systems is illustrated in figure 4.

3.1. PIV systems

The flow was seeded with a Rocket Portable Smoke System (model #PS23—1.1 kW) that uses a glycerine-water solution as working fluid and produces droplets with $1 \mu\text{m}$ median diameter. The illumination source for the PIV measurements was a Photonics Industries laser (model DM40-527) with pulse energy of 40 mJ at 1 kHz. The laser light sheet thickness was set to 1.7 mm and measured by traversing a photodiode. Both PIV systems collected data using a timing sequence commonly referred to as time-series mode (TSM), as shown in figure 5. In TSM acquisition, N images are collected using a continuous rate mode, where the time separation Δt between two successive images is the inverse of the acquisition frequency. The first velocity field is obtained from the interrogation of images 1 and 2, the second velocity field from images 2 and 3, and so on. The resulting analysis yields $N - 1$ vector fields for N images. PIV acquisition using TSM and a sufficiently high acquisition frequency

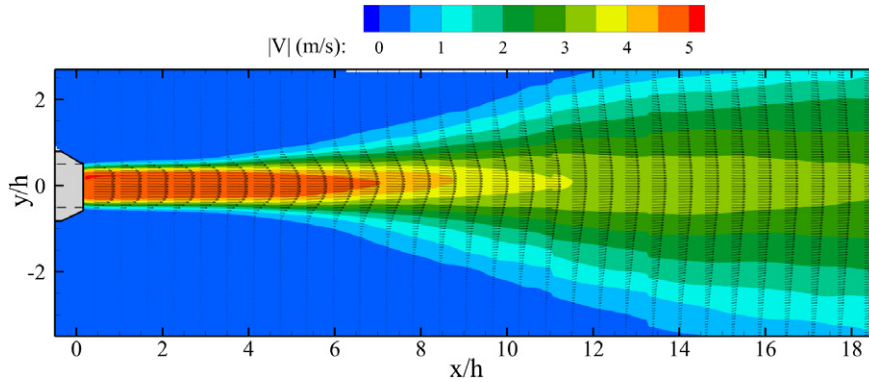


Figure 3. Mean velocity field for the rectangular jet.

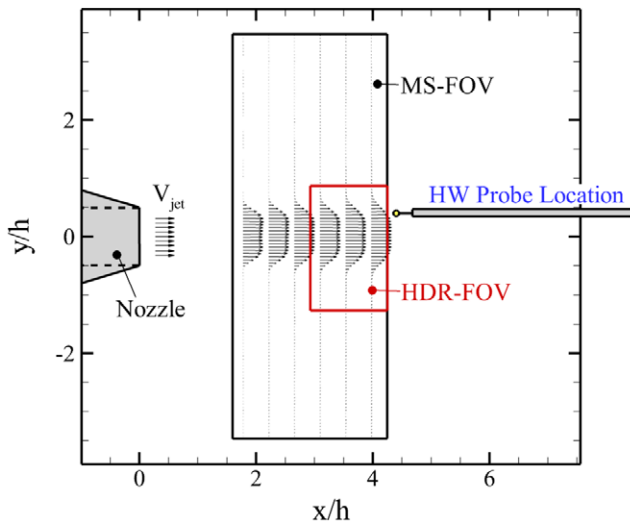


Figure 4. Comparison of the measurement regions for the three systems. FOV indicates the field of view of the PIV systems.

returns velocity fields that are correlated in time. The TSM procedure eliminates errors associated with beam overlap. Another benefit of acquiring PIV data in TSM is that it reduces the effect of possible timing variations inherent in most dual-cavity high-speed lasers (Bardet *et al* 2013), which can yield a significant bias in the measured velocity. These timing anomalies were further reduced by running the diode current of the laser at the upper end of its range. In these conditions, the reported random error (i.e. jitter) is 1.5 ns, and there are no measurable bias errors (Bardet *et al* 2013). As a result, for measurements at 10 kHz the timing error is negligible ($<0.01\%$) with respect to other error sources, such as those associated with the determination of the particles displacement.

3.1.1. Measurement PIV system: PIV-MS. The PIV-MS is based on a single camera that records time-resolved (TR-PIV) images of the particle tracers. The system yields the velocity components within the illuminated plane (2D-2C PIV). A LaVision HighSpeedStar 5 (CMOS, 10 bit, 1024×1024 pixels, $17 \mu\text{m}$ pixel pitch, 3000 frames per second at full resolution) was equipped with a Nikkor 105 mm focal length lens set to $f\# = 4$. The optical magnification of the system was 0.122, leading to a digital imaging resolution of 7.2 px mm^{-1} . The

typical size of the particle images was about 1.5 px and was regulated by slightly shifting the focal plane of the camera.

3.1.2. High dynamic range PIV system: PIV-HDR. The PIV-HDR system was a two camera time-resolved (TR-PIV) system that could measure 3 components of velocity over a nominally 2D light sheet. The two cameras were LaVision HighSpeedStar 6 (CMOS, 12 bit, 1024×1024 pixels, $20 \mu\text{m}$ pixel pitch, 5400 frames per second at full resolution) in a stereoscopic configuration (SPIV). Camera #1 was normal to the laser sheet and mounted a Nikkor objective of 105 mm focal length set to $f\# = 5.6$. Camera #2 had an angle of 49 degrees with respect to the laser sheet normal and used a Nikkor 200 mm focal length lens set to $f\# = 5.6$ (see figure 1 for a picture and schematic of the setup). This specific stereo configuration allows for the HDR system to be used either as a 2D-2C PIV system (using only camera #1) or as a SPIV system (using both cameras). The optical magnification was 0.535, leading to a digital imaging resolution of 26.7 px mm^{-1} . The optimal particle image diameter of 2.5–3 px (Raffel *et al* 2007) was achieved by slightly defocusing the images. Note that the PIV-HDR system had a larger digital imaging resolution by about factor 3.7 with respect to the PIV-MS. As a result, a particle image displacement in the physical space is discretized by a larger number of pixels in the image space for the PIV-HDR system than for the PIV-MS. Hence, since the measurement error is approximately independent of the measured displacement, the PIV-HDR system yields lower relative error by about factor 3–4.

3.1.3. PIV data processing. The PIV recordings have been processed with the LaVision DaVis 8.1.6 software. For the measurement system, the single-pair interrogation algorithm was used with final interrogation window of size 16×16 pixels, corresponding to a measurement region of $2.23 \text{ mm} \times 2.23 \text{ mm}$. The HDR system employed the sliding-average correlation algorithm (Sciacchitano *et al* 2012) on a kernel of five image pairs to further reduce the measurement error. The final interrogation window size was 32×32 pixels, corresponding to a measurement region of $1.42 \text{ mm} \times 1.42 \text{ mm}$. For both systems, the overlap factor was set to 75%, except for the vortex roll-up region, where the overlap was increased to 87.5% to further enhance the spatial resolution. Spurious vectors were detected with the universal

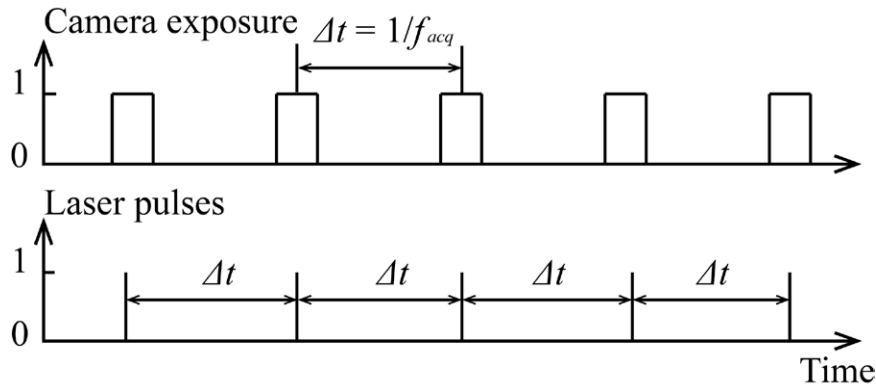


Figure 5. Timing sequence used for the PIV acquisition—time-series mode (TSM). 0: device not active; 1: device active.

outlier detection approach (Westerweel and Scarano 2005), which removed and replaced via linear interpolation of neighboring vectors. No smoothing of the data was performed neither in space nor in time.

3.2. HWA System

The anemometer was a TSI model IFA 300 with 2 channels and 5 m long probe cables. A 16-bit National Instruments A/D board was used to acquire the data. Calibrations were carried out using a TSI manual velocity calibrator model #1129. The reference velocity was measured using pressure taps recording the pressure drop across the nozzle of the calibrator and measured with a Baratron 1-Torr, model #698A. The calibration spanned 5 values of the exit velocity, corresponding to the anticipated velocity range of 1–6 m s⁻¹. The hot-wire calibration equations used a power law transfer function as described in Bruun (1995), where the calibration fit takes the form:

$$E^2 = A + BQ^n \quad (2)$$

In equation (2), E is the voltage output from the anemometer and Q is the effective cooling velocity that is imposed by the calibration facility. A , B , n then become fitting coefficients. This is a modification to the calibration suggested by Collis and Williams (1959), who demonstrated that King's Law ($n = 0.50$) could be improved upon by using $n = 0.45$. Later researchers (several different groups, as noted in Bruun 1995) treated n as a variable, where the value of n that minimized the error of the calibration fit was chosen for each hot-wire calibration (n typically ranged between 0.4–0.45). This modification to the calibration method of Collis and Williams (1959) was also used in the present study and the values for n were allowed to vary between 0.3–0.7. The error for the calibration fits, described by the norm of residuals, was typically 0.0001–0.0005.

The calibrator had the additional capability to change the yaw angle of the probe relative to the flow for use with multi-wire probes (X-probes for this study). The yaw angle positions could be adjusted manually in increments of 6°. X-probe calibrations were carried out using the approach described by Tropea *et al* (2007). The calibration functions take the form:

$$E^2 = A(\gamma) + B(\gamma)Q^{n(\gamma)} \quad (3)$$

Where the yaw angle, γ , was varied over the range ($-36^\circ \leq \gamma \leq +36^\circ$) in increments of 6°, resulting in 13 different sets of A , B , n for each sensor of the X-probe (2 sensors per probe). The data reduction for the X-probe data also followed the approach found in Tropea *et al* (2007).

Several different probe types were used, depending on the required type of data.

- **5 μm single wire normal probes (SN-probes)**

These probes were designed and built by the Turbulent Shear Flows Laboratory (TSFL) of Michigan State University (MSU). The active sensor was a 5 μm diameter tungsten wire with a 1 mm active sensor region. The total wire length was 3 mm, but the outer edges (approximately 1 mm on each side) were copper-plated to isolate the active sensor from aerodynamic effects of the prongs, following the recommendations of Strohl and Comte-Bellot (1973). The active sensor had a length-to-diameter ratio $L/D = 200$.

- **5 μm cross wire probes (X-probes)**

These probes were similar to the 5 μm SN-probes described above, but were composed by two tungsten sensors arranged in a 90° array to measure two orthogonal velocity components. They were also designed and built by the TSFL-MSU. In the experiment, the probe was oriented in such a way to measure the streamwise (u) and transverse (v) velocity components.

- **50 μm SN-probes (TSI model 1210–20)**

This commercially available probe used active sensors made of 50 μm diameter ceramic cylinder coated with platinum ($L/D = 10$; see figure 6(left)).

- **50 μm X-probes (TSI model 1241-20)**

The two active sensors (as above) were oriented in a 90° array, as illustrated in figure 6(right).

Table 1 summarizes the measurement regions of the four probes.

The choice of probe depended on the type of measurement required (single component data, 1C, or two component, 2C). SN-probes are sensitive to both the streamwise (u) and the transverse (v) velocity components, which yield a velocity magnitude in the plane normal to the wire orientation. These probes were used for regions where the velocity was primarily

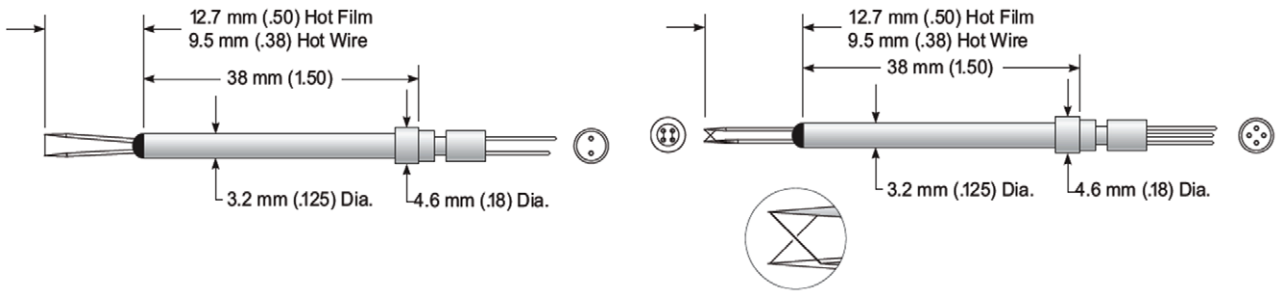


Figure 6. Schematics of the hot-film probes (left: SN-probe; right: X-probe).

Table 1. Measurement regions of the four hot-wire probes.

Probe type	Size of measurement region
MSU TSFL SN-probe	$5\ \mu\text{m} \times 1\ \text{mm}$
MSU TSFL X-probe	$0.7\ \text{mm} \times 0.7\ \text{mm}$
TSI 1210-20 SN-probe	$50\ \mu\text{m} \times 0.5\ \text{mm}$
TSI 1241-20 X-probe	$1.2\ \text{mm} \times 1.2\ \text{mm}$

in the streamwise direction. X-probes are able to resolve the individual streamwise (u) and transverse (v) velocity components separately and were used where the flow was expected to exhibit a significant transverse component, but where the mean and fluctuating spanwise (w) components were small. Restricting the usage of these probes to the nominally 2D regions of the jet provides more details on the streamwise and transverse velocity components (measured directly with PIV), while avoiding the effects of bi-normal cooling on the probes as reported by Zhao and Smits (2006).

The cylindrical platinum film sensors are known to be less susceptible to contamination because of their larger diameter. The possible sources of contamination for the present study are discussed in detail in section 4. The drawback of using the cylindrical platinum film sensors is the lower sensitivity and narrower frequency response caused by the larger sensor mass. Nevertheless, Lekakis (1996) found that these sensors compared quite favorably to smaller diameter sensors in measuring turbulent flows up to 10kHz, which was the upper limit of frequency content in the present experiments. Measurements were carried out with both a single-sensor hot-wire and hot-film probe in a turbulent region of the jet ($x/h = 19.6$, $y/h = 0.0$) to estimate the spectral response of each sensor. The velocity spectra for this turbulent region are shown in figure 7. The spectral content of the hot-film and hot-wire data are quite similar with a slight roll-off of the hot-film data as compared with the hot-wire data. This high frequency roll-off is a directly consequence of the larger diameter of the hot-film probe. Additionally, the hot-film probe shows higher frequency noise spikes for $f > 2\text{kHz}$. Based on these results, different sensors were used for different physical regions of the flow, depending on the anticipated velocity scales and intended use of the data. However, the results shown in the subsequent sections are hot-film data because of their adequate frequency response and resiliency to the seeded environment.

The temperature of the jet was measured using a type K thermocouple. The temperature was sampled at the same time

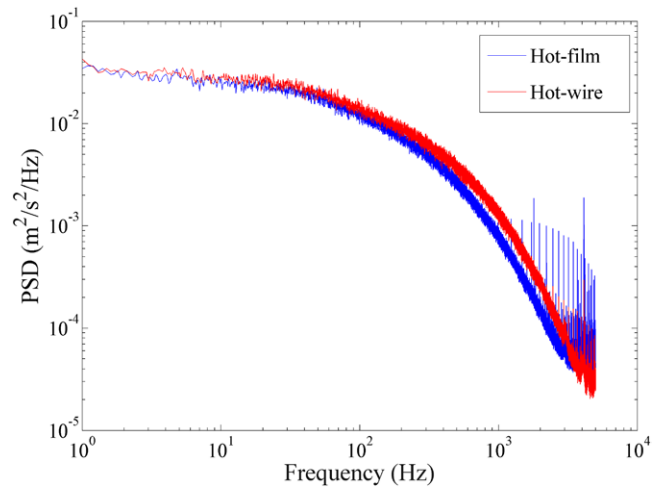


Figure 7. Velocity spectrum of hot-wire compared to hot-film probe at $x/h = 19.0$ and $y/h = 0.0$ (data sampled at 10kHz).

as the hot-wire signal in a location in close proximity to the position of the probe.

4. Considerations for using the HW measurements to verify the PIV-HDR system

An additional measurement system is used to verify the accuracy of the PIV-HDR data. HWA is selected over other techniques (Pitot tube, laser Doppler velocimetry) for its high sensitivity to turbulent fluctuations, the high temporal response and the ease of uncertainty estimation. Moreover, the measurement principle of HWA is independent from particle tracers, making it well-suited as an independent measurement system for verification. A previous study by Mattern *et al* (2012) used simultaneous TR-SPIV and laser Doppler velocimetry (LDV) systems for collecting data in the wake of an axial fan. The authors noted that the PIV measurements were contaminated by the LDV laser beams being visible in the PIV images, which precluded the correct velocity estimation at the LDV measurement location. Conversely, the PIV lasers corrupted the LDV time series producing high-frequency bursts. An additional complexity arose from the fact that LDV time series are not regularly sampled in time, due to the random arrival times of particles within the measurement volume. This makes synchronizing the two measurement techniques even more difficult. HWA has no such limitation and can be

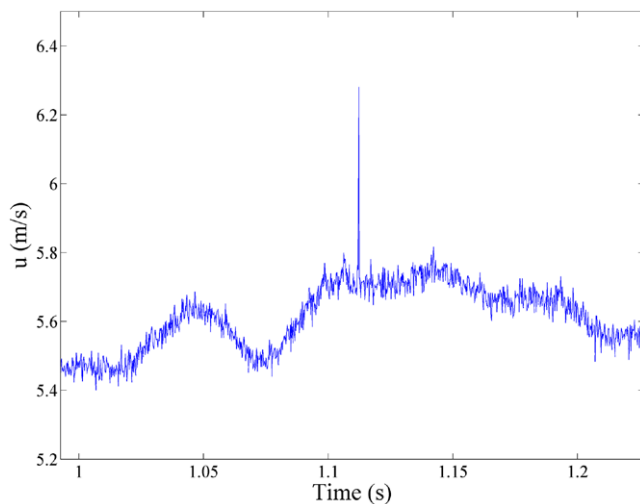


Figure 8. Time series showing a high frequency spike from PIV seeding on hot-wire probe.

easily synchronized to sample at the same intervals as the TR-PIV system. However, using HWA simultaneously with PIV requires some careful considerations to ensure the quality of the comparison.

4.1. Effect of particle seeding on hot-wire and hot-film probes

Initial tests were conducted to determine the effect of seeding particles on the performance of the hot-wire and hot-film probes. Tests with various seeding densities ($0.3\text{--}6\text{ particles/mm}^3$) were conducted while operating the probe both independently of the laser and simultaneously with the laser. Previous works from Falco (1980) and by Klewicki and Hirschi (2004) had examined the effects of simultaneous flow visualization and hot-wire anemometry in turbulent flows. Klewicki and Hirschi (2004) noted that the main adverse effect from the oil fog was the appearance of high-frequency spikes in the hot-wire signals. These spikes were caused by the oil droplet impacting on the wire and then evaporating, resulting in an instantaneous cold spot on the surface of the wire. However, both of these studies were for seeding densities intended for flow visualization, which are considerably higher than those required for PIV measurements. An examination of the time series data for the present study reveals an occasional high frequency spike for hot-wire data collected in the presence of fogging fluid. An example of spike appears in figure 8.

These spikes were found in only a few of the datasets that used the $5\mu\text{m}$ tungsten sensors, which is a direct result of the much lower seeding density used for PIV experiments. Since these spikes are isolated, they can be easily removed via careful data post-processing, e.g. with a median filter. As mentioned in section 3.2, cylindrical platinum hot-film sensors are known to be less susceptible to contamination due to their larger thermal capacity. No high frequency spikes were found for any of the datasets that used the larger diameter $50\mu\text{m}$ platinum sensors.

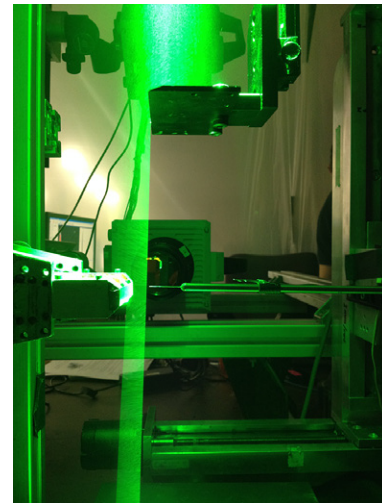


Figure 9. Proximity of the HW probe to PIV illumination sharply delimited with a knife-edge.

4.2. Effect of laser light on hot-wire and hot-film probes

Hot-wire probes may be sensitive to radiative heat transfer too. Therefore, the intense laser illumination is detrimental to their performance. Direct laser light onto the hot-wire sensors causes erroneous readings and possible changes in the calibration. On the other hand, the scattered laser light from the hot-wire would introduce very bright spots potentially damaging the CMOS camera and posing difficulties in locating the hot-wire relative to the PIV measurement plane. The hot-wire sensor is placed at the edge of the illuminated domain. The operation is accurately realized introducing a knife-edge, with the HW probe placed approximately 1.0 mm downstream of the light sheet edge, as shown in figure 9.

4.3. Uncertainty of the hot-wire data

Estimates of the typical uncertainty of the hot-wire data are presented in this section. In addition to the error sources described in sections 3.2, 4.1 and 4.2, there are two other major sources of uncertainty:

- Calibration errors
- Precision uncertainty of the mean quantities (convergence)

The precision uncertainty is important when analyzing and comparing statistical quantities, as discussed by Coleman and Steele (2009) and Wilson and Smith (2013a, 2013b). The primary focus of this work is to create a database for evaluating the uncertainties associated with the instantaneous velocity fields from PIV, so mean and other statistical quantities are not analyzed. The uncertainty related to calibration errors have been estimated for this work using the procedures presented by Yavuzkurt (1984) and Moffat (1985, 1988). These are treated as bias errors and are less than 1%. Additional calibration errors were found by examining the level of agreement of the pre- and post-calibrations for each dataset. Calibrations of the hot-wire were carried out directly before (pre) and after (post) each dataset, as recommended by Tropea

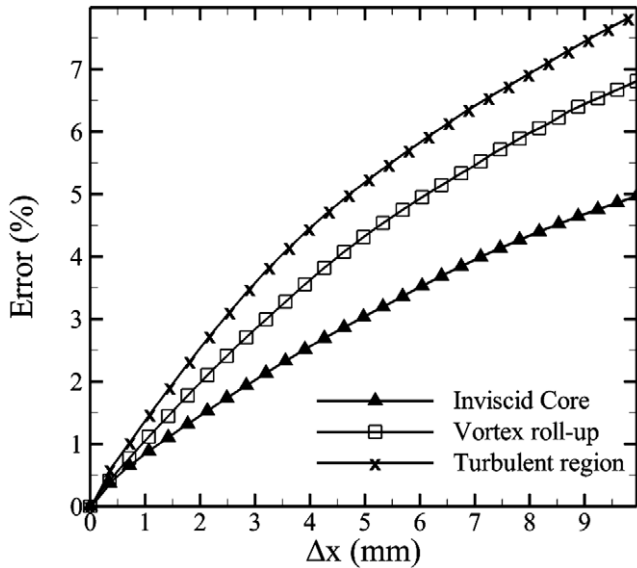


Figure 10. The *rms* error from invoking Taylor's 'frozen flow' hypothesis for increasing spatial separation between the measured points and for different flow regimes.

et al (2007). Any changes in the operating resistances of the probes that were experienced during the data collection will result in a change in the hot-wire and hot-film calibrations. Changes in the operating resistances can be caused by residual strain effects from moving the probes during the experiments (between the calibration rig and the experiment). As discussed in the previous sections, this experiment also had the possible effects of both seeding particles and/or laser light impacting the active sensor of the probes. The pre-post calibration drift was noted for each of the experiments and was found to be 0.5%–1.0% for the majority of the experiments. Calibration errors associated with the pre-post drift were therefore determined to be the largest source of uncertainty. The previous work from Wilson and Smith (2013b) had estimated the uncertainty of their instantaneous hot-wire measurements to be 2.5%; however, they did not compensate for changes in the fluid temperature for each instantaneous measurement. The use of temperature compensation in hot-wire measurements can significantly improve the accuracy of the results (Abdel-Rahman *et al* 1987). The hot-wire data presented here were compensated for variations in temperature using the method proposed by (Abdel-Rahman *et al* 1987).

4.4. Comparisons of HWA and PIV-HDR

In order to establish the PIV-HDR as the 'reference measurement', a comparison is made between the HWA data and the PIV-HDR. Since HWA is a point measurement, a single location in the PIV-HDR domain (directly upstream of the HW probe) is selected. The separation between hot-wire probe and PIV measurement domain was typically 1–2 mm for each of the experiments. An approach invoking Taylor's frozen flow hypothesis is employed, based on the assumption that the flow structures travel at a convective velocity U_c (Taylor 1938):

$$\frac{\partial(\overline{u^2})}{\partial x} = \frac{1}{U_c} \frac{\partial(\overline{u^2})}{\partial t} \quad (4)$$

In equation (4), $\overline{u^2}$ is the mean squared velocity fluctuation along the streamwise direction x (an analogous equation could be written for the transversal direction by substituting u with v). This convective velocity U_c is determined from the correlation of the velocity time-series at two points of the PIV-HDR field, following the approach proposed by Wills (1964).

The velocity measured by the hot-wire at the location (x_{HW}, t) is compared with the velocity from the PIV system (either HDR or MS) at $(x_{\text{PIV}}, t - k\Delta t)$, where $x_{\text{PIV}} = x_{\text{HW}} - U_c k\Delta t$. In this equation, k is the minimum (integer) number of time steps so that x_{PIV} lies inside the PIV domain. Taylor's frozen flow hypothesis is considered an accurate assumption for flows where the amplitude of velocity fluctuations is small relative to the average velocity of the flow (Townsend 1976). The error associated with using Taylor's hypothesis to compare the velocities measured at two different points in space is estimated by extracting time series data from two different points in the PIV-HDR data. The points are separated only in the streamwise direction. The normalized root-mean-square (*rms*) error between the two time series, after shifting the first time series by $k\Delta t$ in the time domain, is shown in figure 10 for different separations Δx and for different regions of the jet. In conclusion, for a spatial separation of 1 mm, the error does not exceed 1%, which translates in a residual discrepancy between the HWA and PIV-HDR time series.

5. Experimental datasets and measurement locations

A series of experiments were carried out in different regions of the rectangular jet. Specific locations were targeted where the flow features pose challenges for the PIV measurements, as illustrated in figure 11. The resulting datasets form a benchmark database with numerous test cases for evaluating PIV uncertainty and advanced PIV processing algorithms.

(a) Steady inviscid jet core ($x/h = 1$ and $y/h = 0$)

The jet core region is characterized by steady potential flow. The SN hot-wire probe was positioned at the jet centerline. The seeding density was varied within the range {0.3, 0.9, 1.8, 3.0 particles/mm³}. The numerical aperture of the PIV-MS system was also varied ($f\# = \{2.8, 4, 5.6, 8\}$) throughout the tests. The latter parameter is important to study the effect of varying the particle image diameter in relation to the peak-locking effect.

(b) Laminar shear layer of the jet ($x/h = 1$ and $y/h = 0.4$)

Within the shear layer close to the jet exit the flow is still steady, but the velocity gradient has an important component across the shear layer. Under these conditions, the measurement errors can be dominated by the effect of particle pattern deformation as well as by the lack of spatial resolution.

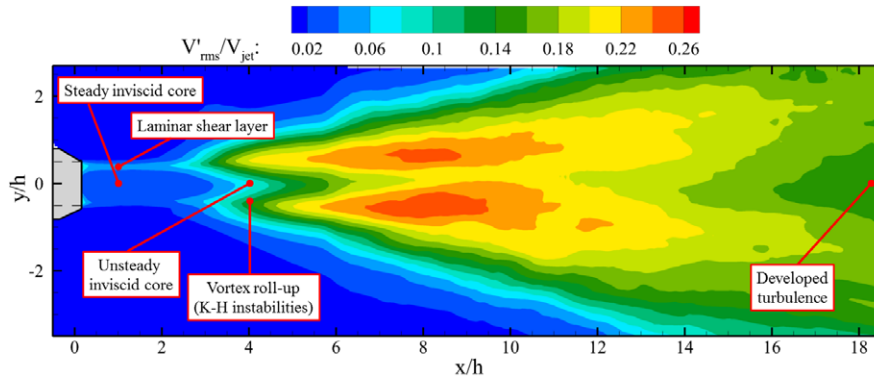


Figure 11. Magnitude of the x - and y -Reynolds stress and overview of the measurement regions.

Table 2. Overview of datasets used to calculate turbulent spectra.

Dataset	Sampling frequency [Hz]	Number of samples
Hot-film/hot-wire	30 000	1 200 000
PIV-HDR	10 000	20 000
PIV-MS	10 000	20 000

(c) Unsteady inviscid jet core ($x/h = 4$ and $y/h = 0$)

In this region, a pulsatile motion of the core flow is induced by the Kelvin–Helmholtz vortices that bound the region. This results in an inviscid unsteady flow, with low-frequency velocity fluctuations.

(d) Vortex roll-up region of the jet shear layer ($x/h = 4$ and $y/h = 0.4$)

Beyond the stable region of the free shear layer, the growth of Kelvin–Helmholtz vortices introduces large fluctuations of both the streamwise and transverse velocity components. The flow remains laminar with a quasi-sinusoidal behavior in the transverse component. The instantaneous streamline curvature induced by such effects becomes significant.

(e) Developed jet turbulence ($x/h = 19$ and $y/h = 0, -0.4, -0.5$)

Downstream of the collapse of the potential core, the jet undergoes transition to the turbulent regime. Here the velocity field features more isotropic fluctuations and out-of-plane motion of the particle tracers. The latter, however, remains relatively small when compared to the mean flow velocity (less than 1% of the local mean centerline velocity). In this region, longer time series were recorded with all three measurement systems enabling a converged estimate of the amplitude spectrum of the velocity fluctuations (table 2).

(f) Effect of mean out-of-plane motion ($x/h = 3$ and $y/h = 0$)

The light sheet was purposely rotated around the y -axis by 16° to obtain measurements where the out-of-plane velocity induces a systematic loss of particle pairs (see figure 12). The measurement errors in PIV are known to strongly depend upon the number of lost particle pairs (Nobach and Bodenschatz 2009).

(g) Effect of cross-plane motion ($x/h = 2$ and $y/h = 0$)

In this experiment, the normal to the light sheet is aligned with the primary flow direction (figure 13). In this case, the out-of-plane motion dominates the experimental errors, as discussed by Nobach and Bodenschatz (2009). The effects of out-of-plane motion yield errors that are similar to those from variations in shot-to-shot intensity of the laser or misalignment of the two laser beams. These phenomena can be more generally classified as ‘event mismatch’. The single-cavity laser configuration used for this experiment (as discussed in section 3.1) minimized the effects of shot-to-shot variations and laser misalignment. This allows for the out-of-plane motion to be the sole contributor to errors from event mismatch.

6. Results

6.1. HWA and PIV-HDR in the unsteady inviscid jet core

Figures 14 and 15 show the velocity time histories obtained at $x/h = 4$ and $y/h = 0$, where the flow undergoes periodic oscillations induced by Kelvin–Helmholtz instability.

A typical example of a time series for the location $x/h=4$, $y/h=0$ is shown in figure 14. Both the HWA and PIV-HDR record the fluctuating velocity in this region in a similar manner. The measured large scale frequency corresponds to a Strouhal number $St = 0.39$, which is consistent with the value reported by Krothapalli *et al* (1981) for their jet flow (aspect ratio of 16.7 and $Re = 12,000$).

The discrepancy between PIV-HDR and HWA data is computed as the difference between the time series of the two systems. A comparison of the absolute and relative *rms* discrepancy and the correlation coefficient between the two time series is shown in table 3. The discrepancy is 1.6% of the local time-averaged velocity. Note that, based on the results of section 4.4, a discrepancy of about 1% may be ascribed to the different spatial locations of HWA and PIV measurement points.

The cross-correlation function between HWA and PIV-HDR time series is computed and shown in table 3. The correlation coefficient approaching 99% indicates a rather good agreement between the two measurements.

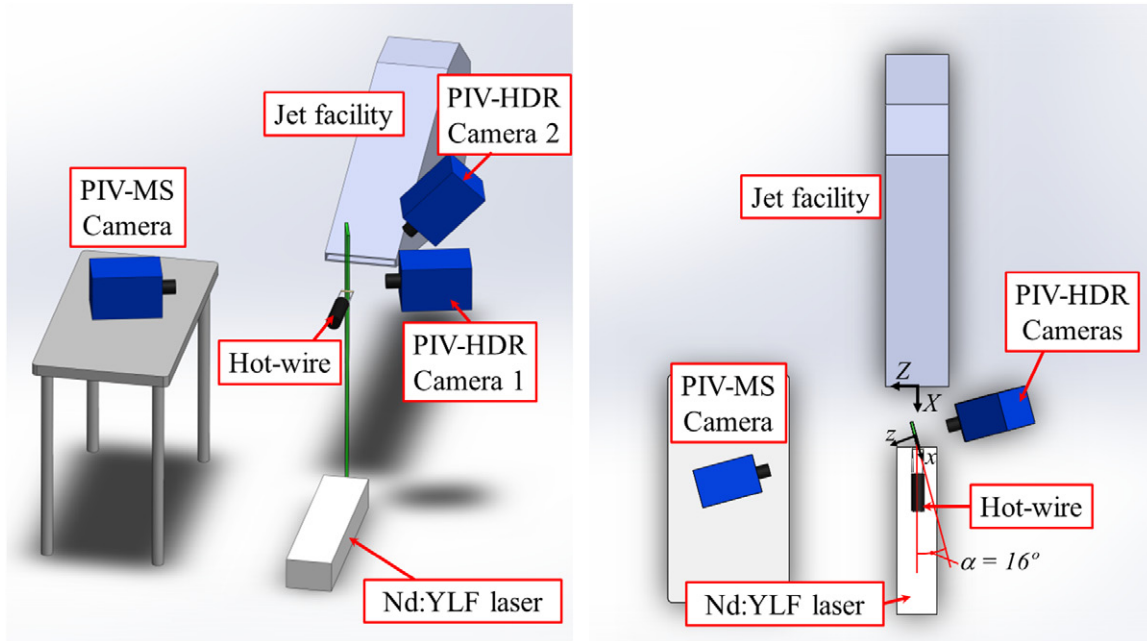


Figure 12. Experimental configuration to study the effects of mean out-of-plane motion (left: perspective view; right: top view).

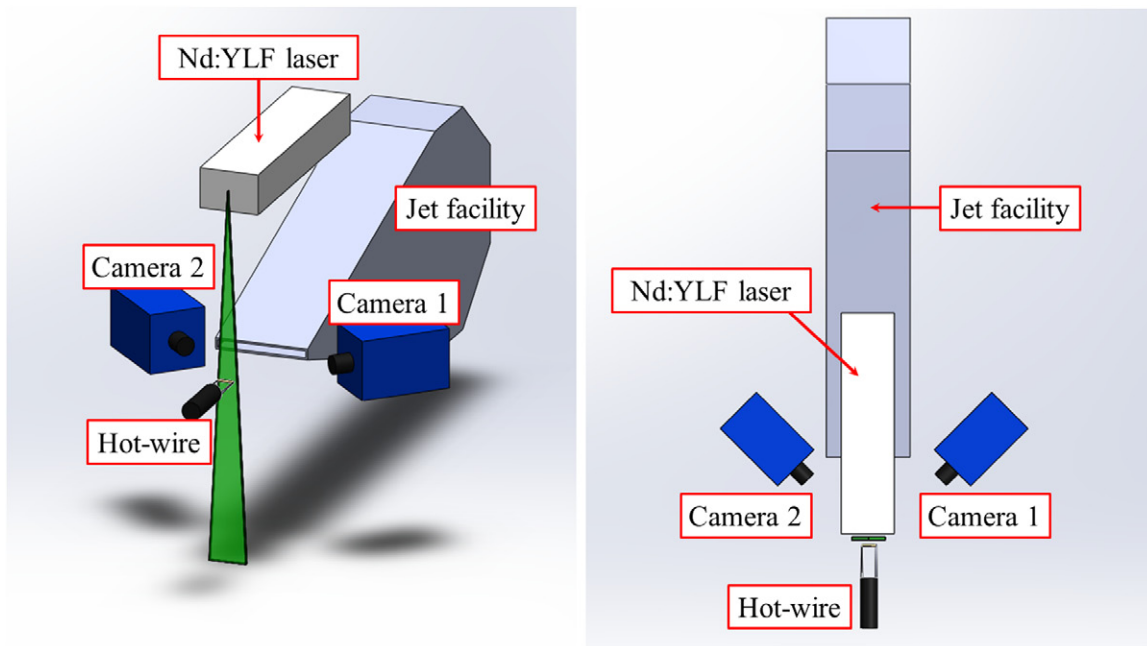


Figure 13. Experimental configuration to study the effects of cross-plane motion (left: perspective view; right: top view).

Additional data collected at the same location using the hot-film X-probe are also presented. These 2C data are shown in figure 15. As expected, the transverse velocity component (v) is smaller in magnitude than the streamwise velocity (u), but the relative fluctuations are significantly larger. The discrepancy and correlation coefficient for these data are shown in table 4. The absolute and relative discrepancies remain comparable to the 1C data, with the relative discrepancy being slightly higher. The correlation between the streamwise velocities is nominally the same; however, a slightly lower correlation is seen in the transverse components. This lower

correlation is the result of relative higher noise exhibited in the measurement.

6.2. HWA with PIV-HDR and PIV-MS in the unsteady inviscid jet core

The results for the PIV-MS are presented for the same dataset. A snapshot of the time series is shown in figure 16. The PIV-MS data are much noisier than both the PIV-HDR and the HW data, but the large-scale fluctuations are resolved (~ 110 Hz). These large-scale fluctuations correspond to fluctuations with an *rms*

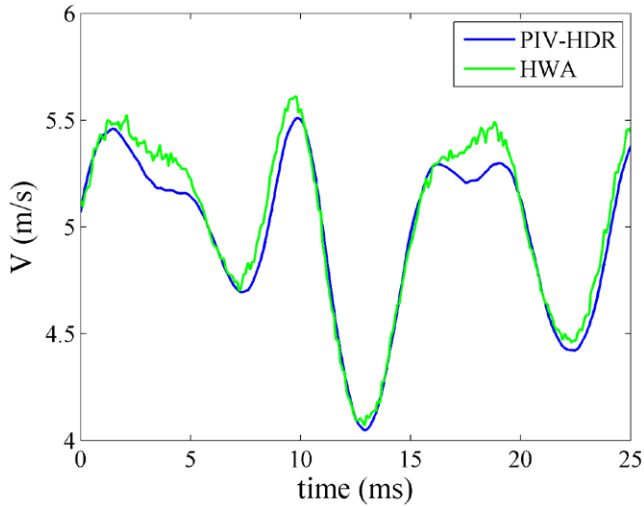


Figure 14. Time series of velocity magnitude from PIV-HDR and HWA (hot-film SN-probe) systems at $x/h = 4$, $y/h = 0$.

amplitude greater than 1 m s^{-1} , while the high frequency *rms* fluctuations from noise exceed 0.2 m s^{-1} . The discrepancy and correlation coefficient (relative to the HWA data) are shown in table 5. The results show that the discrepancy is increased by a factor exceeding 2 with respect to the PIV-HDR system. The correlation coefficient is significantly reduced, but still above 90%. Figure 17 and table 6 show the 2C results for the PIV-MS against the PIV-HDR and the HWA. The results confirm the lower accuracy of the PIV-MS with respect to the PIV-HDR system. In particular, a major reduction of the value of the cross-correlation coefficient of the transverse velocity component is noted.

6.3. Results from other regions

Sections 6.1 and 6.2 have shown that the random noise levels between HWA and PIV-HDR are similar, as seen by the correlation coefficient of 98.7% in table 3. The PIV-MS is also able to measure the large-scale features of the flow field, but its overall relative noise levels are significantly higher. The following sections extend the analysis by examining the performance of these three systems in several different flow fields with increased complexities that pose challenges for any measurement system.

6.3.1. Vortex roll-up region. This region extends the challenges of the unsteady inviscid jet core by moving the measurement regions into the jet shear layer, but still remaining where Kelvin–Helmholtz instabilities are generated. These instabilities lead to large fluctuations of both the streamwise and transverse velocity components. The presence of gradients from the shear layer creates an additional complexity for each of the measurement techniques. In this region, a hot-film X-probe is again used to measure both the streamwise and transverse velocities.

Time-series data for the three systems are shown in figure 18. The streamwise velocity (left) is lower than the core velocity due to shifting the measurement region in the

Table 3. Discrepancy between PIV-HDR and HWA (hot-film SN-probe) data.

Jet region	Absolute discrepancy: d_{rms}	Relative discrepancy: d_{rms}/V	Cross-correlation coefficient
Unsteady inviscid jet core ($x/h = 4$, $y/h = 0$)	0.082 m s^{-1}	1.6%	98.7%

transverse direction. Here the relative fluctuations are considerably higher (30% or more of the free-stream velocity). The overall absolute discrepancy (d_{rms}) for the streamwise velocity is also higher (see table 7). The correlation between the PIV-HDR and HWA exceeds 90%. The correlation for the PIV-MS and HWA is lower, which is a direct result of the higher noise in data. The right-hand side of figure 18 shows the transverse velocity, which has large fluctuations over a nominally zero mean velocity.

6.3.2. Effect of mean out-of-plane motion. The effect of mean out-of-plane motion on a PIV measurement is assessed using data collected from the experimental configuration shown in figure 12. The measurement region was in the inviscid region at $x/h = 2$, $y/h = 0$, which is close to the unsteady inviscid jet core region, thus some unsteadiness is expected.

The mean in-plane velocity measured by the two PIV systems is approximately 4.7 m s^{-1} , corresponding to an in-plane displacement of approximately 1.2 mm between succeeding PIV images. The out-of-plane velocity is 1.3 m s^{-1} , which yields a z -displacement of approximately 18% of the laser sheet thickness. A snapshot of the time series is shown in figure 19.

Each of the three systems is able to track the low-frequency variations of the flow field, but the PIV-MS shows considerably higher random noise fluctuations than the other two measurements. To evaluate the contribution only of the random error component, the analysis is conducted after subtracting from each time series the sliding-average value over a kernel of 25 ms, which is comparable with the integral time scale of the signal. The result of this analysis are summarized in table 8: the PIV-HDR system yields random discrepancy well below 1% of the local mean velocity and is more accurate than the PIV-MS system by almost a factor 4. The cross-correlation coefficient between PIV and HW is 90% when using the PIV-HDR system and 68% when using the PIV-MS.

6.3.3. Developed turbulence region. A region of developed turbulence ($x/h = 19.0$ and $y/h = 0.0$) exists further downstream from the previous measurement points. In this region, a large range of turbulent velocity scales is expected. Here the temporal response of the hot-wire provides a good reference condition for evaluating the spectral response of the PIV systems.

The power spectral densities for the three systems are shown in figure 20. The HWA spectrum spans over five decades and does not show any significant high frequency roll-up since it is passed through an analog filter before it is digitally sampled. The PIV-HDR spectrum is consistent with

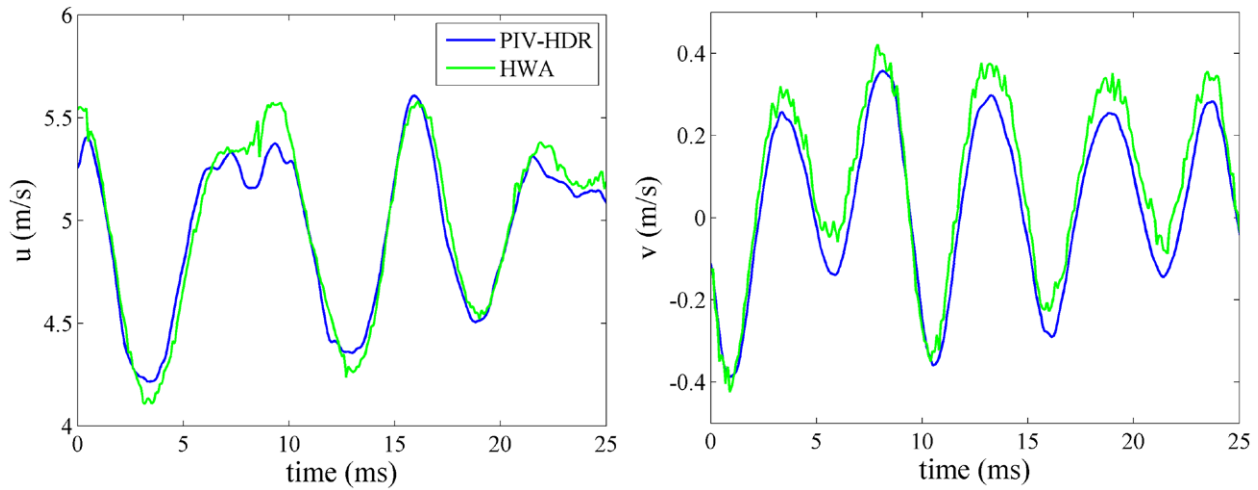


Figure 15. Velocity time series from PIV-HDR and HWA at $x/h = 4, y/h = 0$ (hot-film X-probe; left: streamwise velocity component; right: transverse velocity component). The legend applies to both plots.

Table 4. Discrepancy between PIV-HDR and HWA (hot-film X-Probe) data.

Jet region	Absolute discrepancy: d_{rms}		Relative discrepancy: d_{rms}/V		Cross-correlation coefficient	
	u	v	u	v	u	v
Unsteady inviscid jet core ($x/h = 4, y/h = 0$)	0.099 m/s	0.055 m/s	2.0%	1.1%	98.7%	96.3%

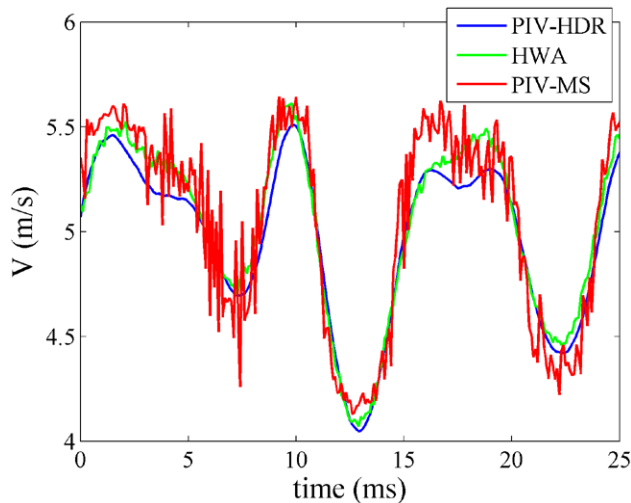


Figure 16. Time series of velocity magnitude from PIV-HDR, HWA (hot-film SN-probe) and PIV-MS systems at $x/h = 4, y/h = 0$.

Table 5. Discrepancy between PIV-MS and HWA (hot-film SN-probe) data.

Jet region	Absolute discrepancy: d_{rms}	Relative discrepancy: d_{rms}/V	Cross-correlation coefficient
Unsteady inviscid jet core ($x/h = 4, y/h = 0$)	0.170 m/s	3.40%	93.2%

the hot-wire, but exhibits a high-frequency roll-up at a frequency exceeding 2000 Hz ($PSD \approx 4 \cdot 10^{-8} m^2 s^{-2} Hz^{-1}$). Such behavior is characteristic of data that cannot resolve

the entire frequency range over which it has been acquired, and is caused by aliasing of the high frequency noise. The power spectrum for the PIV-MS follows the same trend as the previous two, but it shows a high frequency roll-up at lower frequency with respect to the PIV-HDR system, that is 1000 Hz ($PSD \approx 10^{-6} m^2 s^{-2} Hz^{-1}$). This result suggests that the PIV-MS is affected by higher noise magnitude than the PIV-HDR system and is unable to resolve the flow fluctuations in a larger range of frequencies.

A portion of the velocity time-series is shown in figure 21. HWA and PIV-HDR measurements are consistent with each other, whereas the PIV-MS exhibits high-frequency fluctuations of the order of $0.5 m s^{-1}$ ascribed to measurement noise. The results of table 9 show the high degree of correlation between HWA and PIV-HDR system (95.8%). The use of the PIV-MS causes a drop of the correlation (92.6%) and an increase in the discrepancy with respect to the HWA data.

6.4. Effect of cross-plane motion

An additional dataset designed to evaluate the effects of cross-plane motion in stereoscopic PIV is also presented. This dataset differs from the previous ones because only one PIV system was employed, which corresponds to the PIV-HDR system of the previous cases. The PIV measurements were acquired in stereoscopic configuration. The HWA system used a SN hot-film probe placed directly downstream of the light sheet as shown in figure 13.

Figure 22(left) shows the velocity magnitude in the xy -plane (i.e. streamwise-transverse) for both the HWA and the PIV systems. This quantity is computed since the SN-probe does not measure a single component of velocity but rather a

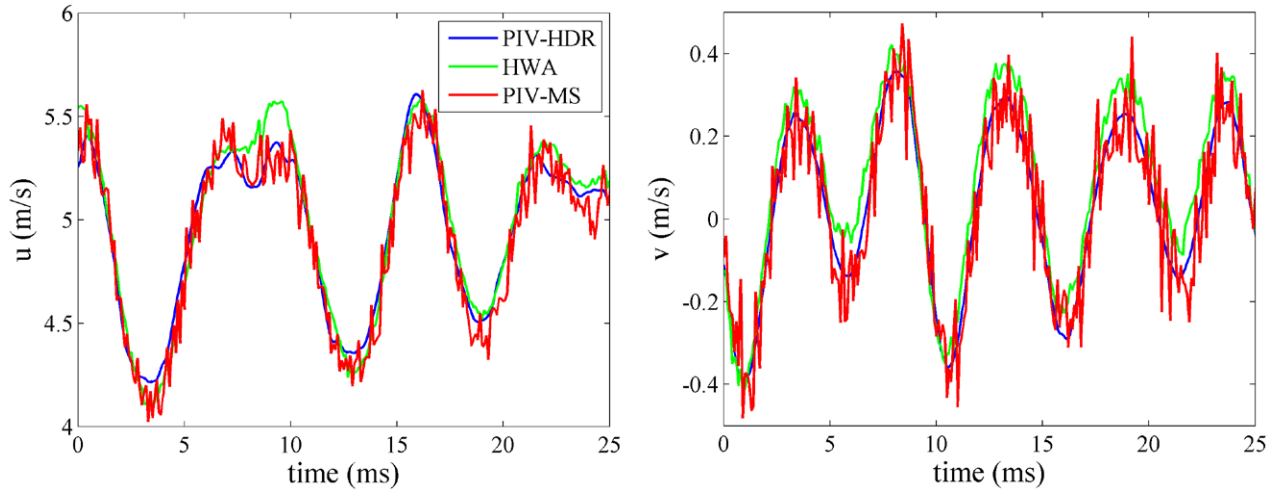


Figure 17. Velocity time series from PIV-HDR, HWA (hot-film X-probe), and PIV-MS at $x/h = 4$, $y/h = 0$ (left: streamwise; right: transverse). The legend applies to both plots.

Table 6. Discrepancy between PIV-MS and HWA (hot-film X-probe) data.

Jet region	Absolute discrepancy: d_{rms}		Relative discrepancy: d_{rms}/V		Cross-correlation coefficient	
	u	v	u	v	u	v
Unsteady inviscid jet core ($x/h = 4$, $y/h = 0$)	0.10 m/s	0.08 ms^{-1}	2.1%	1.6%	96.8%	77.1%

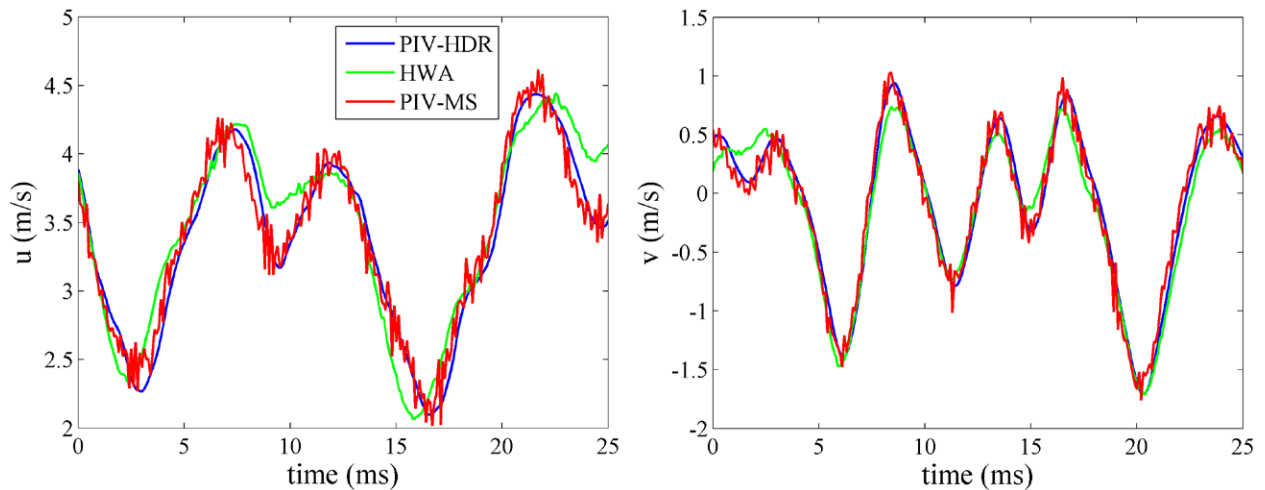


Figure 18. Velocity time series from PIV-HDR, HWA (hot-film X-probe) and PIV-MS at $x/h = 4$, $y/h = 0.4$ (left: streamwise; right: transverse). The legend applies to both plots.

Table 7. Discrepancy for the PIV-HDR and PIV-MS systems with respect to the HWA (hot-film) X-probe in the region of Kelvin–Helmholtz vortices roll-up ($x/h = 4$, $y/h = 0.4$).

System	Absolute discrepancy: d_{rms}		Relative discrepancy: d_{rms}/V		Cross-correlation coefficient	
	u	v	u	v	u	v
PIV-HDR	0.173 ms^{-1}	0.108 ms^{-1}	5.0%	3.1%	91.9%	98.6%
PIV-MS	0.243 ms^{-1}	0.143 ms^{-1}	7.0%	4.1%	88.1%	97.4%

velocity magnitude in the plane normal to the orientation of the active sensor.

The measurements are collected in the inviscid jet core ($x/h = 2$ and $y/h = 0$), where the turbulence intensity is expected to be under 2% (Wilson and Smith 2013b). The

freestream turbulence intensity measured by the HWA system is considerably lower than that measured by PIV (1.7% versus 2.9%); the root-mean-square of the difference between PIV and HW results is 0.12 ms^{-1} , which corresponds to 2.6% of the local time-averaged velocity. The PIV analysis is repeated

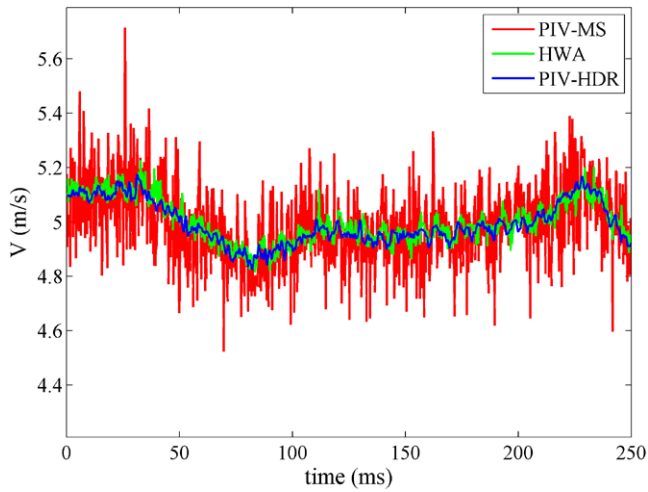


Figure 19. Velocity magnitude time series from PIV-HDR, HWA (hot-film SN-probe) and PIV-MS systems when measuring a flow with non-null mean out-of-plane motion (at $x/h = 2$, $y/h = 0$). A small bias error (2% of the jet velocity) between HWA and PIV data has been corrected. This bias error is ascribed to hot-wire pre-post calibration drift and to the uncertainty ($\pm 0.5^\circ$) in the measurement of the laser sheet angle with respect to the jet exit direction.

Table 8. Random discrepancy for the PIV-HDR and PIV-MS systems compared with SN-Probe.

System	Absolute discrepancy: d_{rms}	Relative discrepancy: d_{rms}/V	Cross-correlation coefficient
PIV-HDR	0.032 m s^{-1}	0.6%	90.0%
PIV-MS	0.116 m s^{-1}	2.3%	68.0%

using an advanced multi-frame interrogation algorithm for time-resolved PIV, namely the sliding-average correlation (Sciacchitano *et al* 2012). A kernel of 5 correlation functions is employed for the sliding-average algorithm. The results of figure 22(right) clearly show that the advanced multi-frame analysis dramatically reduces the random noise in the measurement. The turbulence intensity is reduced to 1.8%, which is consistent with the HW result. The root-mean-square of the difference between PIV and HW velocities drops to 0.07 m s^{-1} , which is 1.5% of the local time-averaged velocity.

6.5. Measurement error of the PIV-MS

The previous sections have demonstrated the good agreement between PIV-HDR and HWA data. Conversely, the PIV-MS time series typically feature larger discrepancy with respect to the HWA time series. Therefore, the PIV-HDR velocity fields can be regarded as a reference because of their higher accuracy (typically by a factor three to four) with respect to the PIV-MS. The measurement error of the PIV-MS is computed as the difference between PIV-MS and PIV-HDR data and summarized in table 10 for the jet regions discussed in sections 6.1–6.3. It is noted that the error typically ranges between 1% and 4% of the local time-averaged streamwise velocity. A thorough discussion of the error sources in these regions is reported in Sciacchitano *et al* (2015).

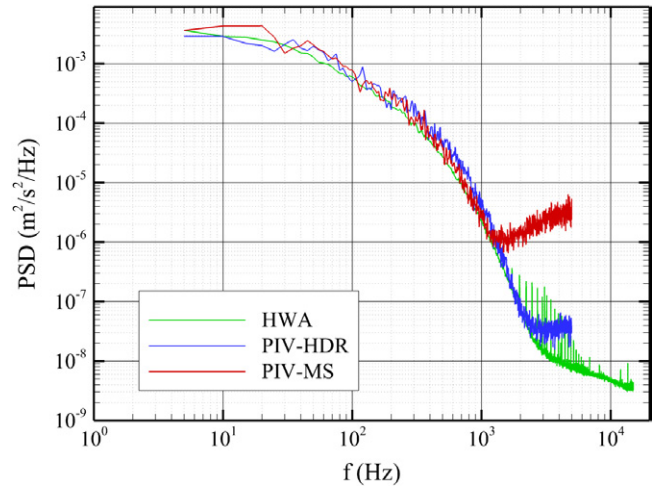


Figure 20. Velocity power spectral densities from hot-film SN-probe (HWA) and the PIV systems at $x/h = 19.0$ and $y/h = 0.0$.

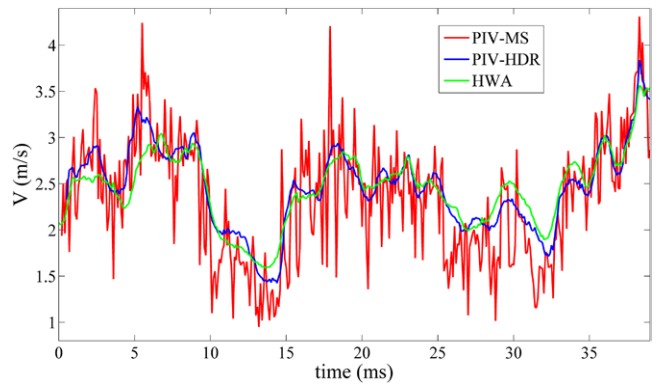


Figure 21. Velocity magnitude time series from PIV-HDR, HWA and PIV-MS systems in the developed turbulence region (at $x/h = 19.0$ and $y/h = 0.0$).

Table 9. Discrepancy for the PIV-HDR and PIV-MS systems with respect to HWA (hot-film SN-Probe).

System	Absolute discrepancy: d_{rms}	Relative discrepancy: d_{rms}/V	Cross-correlation coefficient
PIV-HDR	0.151 m s^{-1}	5.0%	95.8%
PIV-MS	0.194 m s^{-1}	6.4%	92.6%

7. The PIV uncertainty quantification database

The various test cases described in section 5 and examined in greater detail in section 6 are only a part of the overall set of measurements that comprise the PIV uncertainty quantification database. A wide range of measurement parameters were carefully selected and varied in a variety of different flow conditions. The overview of the dataset can be seen in figure 23. Each of the columns (the flow conditions) was measured at some point of the jet flow and is described in sections 5 and 6. Additionally, the measurement parameters (each of the rows) were also systematically varied throughout the measurement campaign. An ‘X’ indicates where a flow condition and a measurement parameter coincide. It should be noted that for each flow condition, there exists a basic dataset where all of the

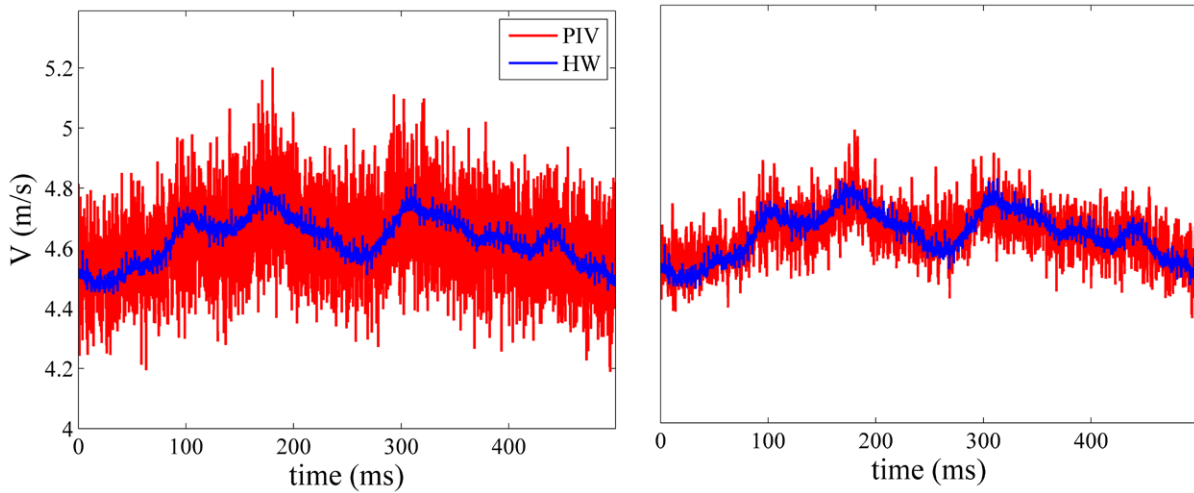


Figure 22. Velocity time series from the hot-film probe and the PIV system for the case of cross-plane motion (left: PIV result computed with standard single-pair correlation; right: PIV result computed with sliding-average correlation).

Table 10. Measurement error of the PIV-MS in the jet regions discussed in section 6.

Jet region	Local streamwise velocity V	Absolute error: ϵ_{rms}		Relative error: ϵ_{rms}/V	
		u	v	u	v
Unsteady inviscid core ^a	4.85 m s^{-1}	0.179 m s^{-1}	0.113 m s^{-1}	3.7%	2.3%
Unsteady inviscid core ^b	4.90 m s^{-1}	0.093 m s^{-1}	0.080 m s^{-1}	1.9%	1.6%
Vortex roll-up shear region	3.38 m s^{-1}	0.102 m s^{-1}	0.094 m s^{-1}	3.0%	2.8%
Jet core: mean out-of-plane motion	4.69 m s^{-1}	0.111 m s^{-1}	0.104 m s^{-1}	2.4%	2.2%
Developed turbulent region	2.99 m s^{-1}	0.110 m s^{-1}	0.095 m s^{-1}	3.7%	3.3%

^a PIV recordings simultaneous with HWA hot-film SN-probe measurements.
^b PIV recordings simultaneous with HWA hot-film X-probe measurements.

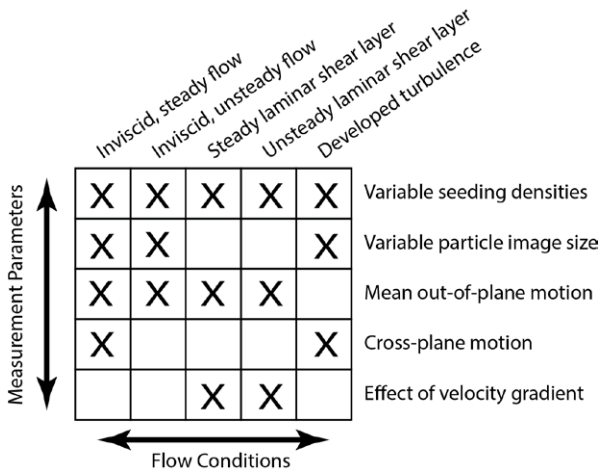


Figure 23. Overview of the test matrix for the PIV uncertainty quantification database.

various measurement parameters were adjusted per best practices for PIV. Several of these cases are used to examine PIV uncertainty quantification methods in Sciacchitano *et al* 2015.

8. Conclusions

An experimental database for evaluating PIV uncertainty quantification methods has been established. This database

covers an extensive range of fundamental flow features that are of interest to many experimentalists using PIV. The parameters of the experiment were carefully controlled such that known error sources for PIV were incorporated and systematically varied. This allows for their effects on PIV accuracy to be investigated using experimental data.

The database is comprised of velocity data collected using three different measurement systems, namely two PIV systems and a hot-wire system. These three systems were successfully synchronized to record simultaneously on a point-by-point basis. They also have a high temporal resolution relative to the flow fields that are being measured (4–10 kHz). The three measurement systems are in good agreement with each other when measuring a variety of different flow conditions, as demonstrated by the high correlations between each. The comparison with the HW data showed that the PIV-MS features significantly higher noise levels, which are consistent with what is found in many PIV experiments. Conversely, the PIV-HDR system is strongly correlated with the HWA system on a point-by-point basis and exhibits noise levels lower by factor three to four than PIV-MS. In some cases, small bias errors exist, which are likely due to bias errors introduced in the HW calibration procedure.

Small velocity discrepancies between PIV and HW data are observed. These are ascribed to the different spatial location of the two measurement systems, the HW probe being

located about 1 mm downstream of the PIV measurement domain. Due to these discrepancies, the HW data shall not be used directly to infer the measurement error of the PIV-MS. Contrary, the HDR data can be used to estimate the PIV-MS error, because HDR and MS velocities are measured at the same spatial locations. The thorough analysis of the PIV-MS error and comparison with the uncertainty provided by different PIV-UQ methods is conducted in a second paper within this volume (Sciacchitano *et al* 2015).

The spectral response of the three systems has been presented. The HWA system, which is known to have a superior temporal resolution, is able to measure over 3.5 decades of the flow when placed in a region with developed turbulence. The PIV-HDR system is able to measure nearly 3.5 decades, whereas the PIV-MS can resolve approximately 3 decades of the flow.

An additional dataset that examines the cross-plane component of velocity from a SPIV system is presented. This dataset was measured using the PIV-HDR system as the ‘test’ system with a SN-probe providing the reference measurement.

The database described in this paper is intended to be publicly available for the general use of the research community for further development, evaluation and benchmarking of PIV UQ methods. Furthermore, these data can also be used in the development of PIV processing and post-processing methods (particularly those used in TR-PIV data). This database is therefore openly accessible through the website: www.piv.de/uncertainty.

References

- Abdel-Rahman A, Tropea C, Slawson P and Strong A 1987 On temperature compensation in hot-wire anemometry *J. Phys. E: Sci. Instrum.* **20** 315
- Bardet P M, André M A and Neal D R 2013 Systematic timing errors in laser-based transit-time velocimetry *10th Int. Symp. on Particle Image Velocimetry—PIV13 (Delft, The Netherlands, 1–3 July 2013)*
- Bruun H H 1995 Hot-wire anemometry *Principle and Signal Analysis* (Oxford: Oxford University Press)
- Charonko J J and Vlachos P P 2013 Estimation of uncertainty bounds for individual particle image velocimetry measurements from cross-correlation peak ratio *Meas. Sci. Technol.* **24** 065301
- Christensen K T 2004 The influence of peak-locking errors on turbulence statistics computed from PIV ensembles *Exp. Fluids* **36** 484–97
- Coleman H W and Steele W G 2009 *Experimentation, Validation, and Uncertainty Analysis for Engineers* 3rd edn (Hoboken, NJ: Wiley) (doi:10.1002/9780470485682)
- Collis D C and Williams M J 1959 2D convection from heated wires at low Reynolds numbers *J. Fluid. Mech.* **6** 357–84
- Falco R E 1980 Combined simultaneous flow visualization/hot-wire anemometry for the study of turbulent flows *J. Fluid. Eng. TASME* **102** 174–82
- Hain R and Kähler C J 2007 Fundamentals of multiframe particle image velocimetry (PIV) *Exp. Fluids* **42** 575–87
- Huang H, Dabiri D and Gharib M 1997 On errors of digital particle image velocimetry *Meas. Sci. Technol.* **8** 1427–40
- Keane R D and Adrian R J 1992 Theory of cross-correlation analysis of PIV images *Appl. Sci. Res.* **49** 191–215
- Klewicki J C and Hirschi C R 2004 Flow field properties local to near-wall shear layers in a low Reynolds number turbulent boundary layer *Phys. Fluids* **16** 4163–76
- Krothapalli A, Baganoff D and Karamcheti K 1981 On the mixing of a rectangular jet *J. Fluid Mech.* **107** 201–20
- Lavoie P, Avallone G, De Gregorio F, Romano G P and Antonia R A 2007 Spatial resolution of PIV for the measurement of turbulence *Exp. Fluids* **43** 39–51
- Lekakis I 1996 Calibration and signal interpretation for single and multiple hot-wire/hot-film probes *Meas. Sci. Technol.* **7** 1313–33
- Lecordier B, Demare D, Vervisch L M J, Réveillon J and Trinite M 2001 Estimation of the accuracy of PIV treatments for turbulent flow studies by direct numerical simulation of multi-phase flow *Meas. Sci. Technol.* **12** 1382
- Lynch K P and Scarano F 2013 A high-order time-accurate interrogation method for time-resolved PIV *Meas. Sci. Technol.* **24** 035305
- Mattern P, Sieber S, Dues M, Caglar S and Gabi M 2012 Simultaneous high speed stereo PIV and LDA measurements in the highly transient vortical wake of an axial fan *16th Int. Symp. on Application of Laser Techniques to Fluid Mechanics (Lisbon, Portugal)*
- Meunier P and Leweke T 2003 Analysis and treatment of errors due to high velocity gradients in particle image velocimetry *Exp. Fluids* **35** 408–21
- Moffat R J 1985 Using uncertainty analysis in the planning of an experiment *J. Fluids Eng.* **107** 173–8
- Moffat R J 1988 Describing the uncertainties in experimental results *Exp. Thermal Fluid Sci.* **1** 3–17
- Nobach H and Bodenschatz E 2009 Limitations of accuracy in PIV due to individual variations of particle image intensities *Exp. Fluids* **47** 27–38
- Raffel M, Willert C, Wereley S and Kompenhans J 2007 *Particle Image Velocimetry—a Practical Guide* 2nd edn (Berlin: Springer)
- Saarenrinne P, Piirto M and Eloranta H 2001 Experiences of turbulence measurement with PIV *Meas. Sci. Technol.* **12** 1904
- Sciacchitano A, Neal D R, Smith B L, Warner S O, Vlachos P P, Wieneke B and Scarano F 2015 Collaborative framework for PIV uncertainty quantification: comparative assessment of methods *Meas. Sci. Technol.* **26** 074004
- Sciacchitano A, Scarano F, and Wieneke B 2012 Multi-frame pyramid correlation for time-resolved PIV *Exp. Fluids* **53** 1087–105
- Sciacchitano A, Wieneke B and Scarano F 2013 PIV uncertainty quantification by image matching *Meas. Sci. Technol.* **24** 045302
- Stanislas M, Okamoto K, Kähler C J and Westerweel J 2005 Main results of the second international PIV challenge *Exp. Fluids* **39** 170–91
- Stanislas M, Okamoto K, Kähler C J, Westerweel J and Scarano F 2008 Main results of the third international PIV challenge *Exp. Fluids* **45** 27–71
- Strohl A and Comte-Bellot G 1973 Aerodynamic effects due to configuration of X-wire anemometers *J. Appl. Mech.* **40** 661
- Taylor G I 1938 Production and dissipation of vorticity in a turbulent fluid *Proc. R. Soc. Lond. A* **164** 15–23
- Timmins B H, Wilson B W, Smith B L and Vlachos P P 2012 A method for automatic estimation of instantaneous local uncertainty in particle image velocimetry measurements *Exp. Fluids*, **53** 1133–47
- Townsend A A 1976 *The Structure of Turbulent Shear Flow* 2nd edn (Cambridge: Cambridge University Press)
- Tropea C, Yarin A L and Foss J F 2007 *Springer Handbook of Experimental Fluid Mechanics* (Berlin: Springer)
- Westerweel J 1997 Fundamentals of digital particle image velocimetry *Meas. Sci. Technol.* **8** 1379–92
- Westerweel J 2000 Theoretical analysis of the measurement precision in particle image velocimetry *Exp. Fluids* **29** S3–12
- Westerweel J 2008 On velocity gradients in PIV interrogation *Exp. Fluids* **44** 831–42

- Westerweel J and Scarano F 2005 Universal outlier detection for PIV data *Exp. Fluids* **39** 1096–100
- Wieneke B 2015 PIV uncertainty quantification from correlation statistics *Meas. Sci. Technol.* **26** 074002
- Wills J A B 1964 On convection velocities in turbulent shear flows *J. Fluid. Mech.* **20** 417–32
- Wilson B M and Smith B L 2013a Taylor-series and Monte-Carlo-method uncertainty estimation of the width of a probability distribution based on varying bias and random error *Meas. Sci. Technol.* **24** 035301
- Wilson B M and Smith B L 2013b Uncertainty on PIV mean and fluctuating velocity due to bias and random errors *Meas. Sci. Technol.* **24** 035302
- Yavuzkurt S 1984 A guide to uncertainty analysis of hot-wire data *J. Fluids Eng.* **106** 181–6
- Zhao R and Smits A J 2006 Binormal cooling errors in crossed hot-wire measurements *Exp. Fluids* **40** 212–7